CRYSTAL GROWTH & DESIGN

pubs.acs.org/crystal

Article

Droplet-Based Evaporative System for the Estimation of Protein Crystallization Kinetics

Moo Sun Hong, Amos E. Lu, Jaehan Bae, Jong Min Lee, and Richard D. Braatz*

Cite This: *Cryst. Growth Des.* 2021, 21, 6064–6075

Read Online

ACCESS | Metrics & More | Article Recommendations | Supporting Information

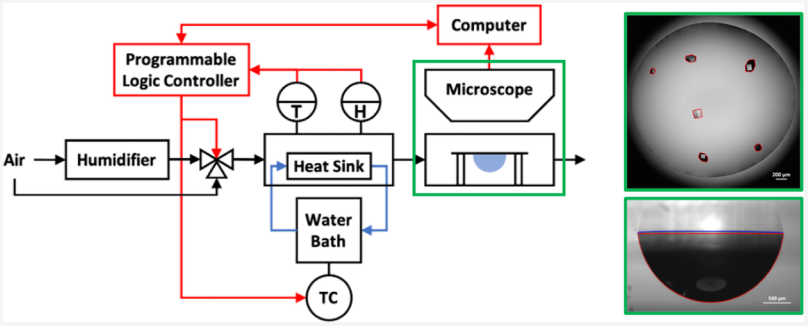

ABSTRACT: Crystallization is a potential cost-effective alternative to chromatography for the purification of biotherapeutic proteins. Crystallization kinetics are required for the design and control of such processes, but only a limited quantity of proteins is available during the initial stage of process development. This article describes the design of a droplet-based evaporative system for the evaluation of candidate crystallization conditions and the estimation of kinetics using only a droplet (on the order of μL) of protein solution. The temperature and humidity of air fed to a flow cell containing the droplet are controlled for evaporation and rehydration of the droplet, which are used for manipulating supersaturation. Dual-angle images of the droplet are taken and analyzed on-line to obtain the droplet volume and crystal sizes. Crystallization kinetics are estimated based on a first-principles process model and experimental data. Tight control of temperature and humidity of the air, fast and accurate image analysis, and accurate estimation of crystallization kinetics are experimentally demonstrated for a model protein lysozyme. The estimated kinetics are suitable for the model-based design and control of protein crystallization processes.

1. INTRODUCTION

Packed-bed chromatography is the most common bioseparation process for biopharmaceutical manufacturing because of its high resolution. However, even with recent technologies for operational improvements including periodic counter-current chromatography, simulated moving bed chromatography, and multi-column counter-current solvent gradient purification,[1] chromatographic purification scales linearly with production rate and is a substantial proportion of the manufacturing costs. Chromatography has become more than half of the cost of goods for some biotherapeutic proteins such as monoclonal antibodies,[2] which will increase as titers and product demands continue to increase.[3−6]

Among alternative non-chromatography separation methods, crystallization is already widely used for the purification of small-molecule pharmaceutical compounds due to its cost-effectiveness. Crystallization has operating costs that scale sub-linearly with throughput.[3,7] Furthermore, crystallization is conducive for the application of process analytical technology during operation. On-line real-time measurements enable model identification, real-time process monitoring, and advanced control implementation. This capability would enable a digital manufacturing approach to be applied in bioseparation in which manufacturing is integrated around a computer system using modern system engineering tools.[3,8]

Crystallization technology for large-molecule therapeutic proteins is much less mature than for small molecules and is mostly still in research and development other than a few isolated products.[1,3,6,7] Protein crystallization is mainly studied by micro-batch scale protein crystallization experiments focused on high-throughput protein crystallization screening for creating single protein crystals large enough for protein structure identification. These studies include the use of robotic systems[9,10] that perform automated mixing and operation, microfluidic systems[11−14] for mixing and encapsulating reagents, evaporation-based systems[15−17] with a precipitant reservoir or pumps for adding precipitant solution

Received: February 28, 2021
Revised: July 11, 2021
Published: October 18, 2021

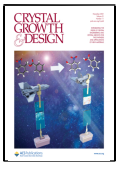

https://doi.org/10.1021/acs.cgd.1c00231
Cryst. Growth Des. 2021, 21, 6064–6075

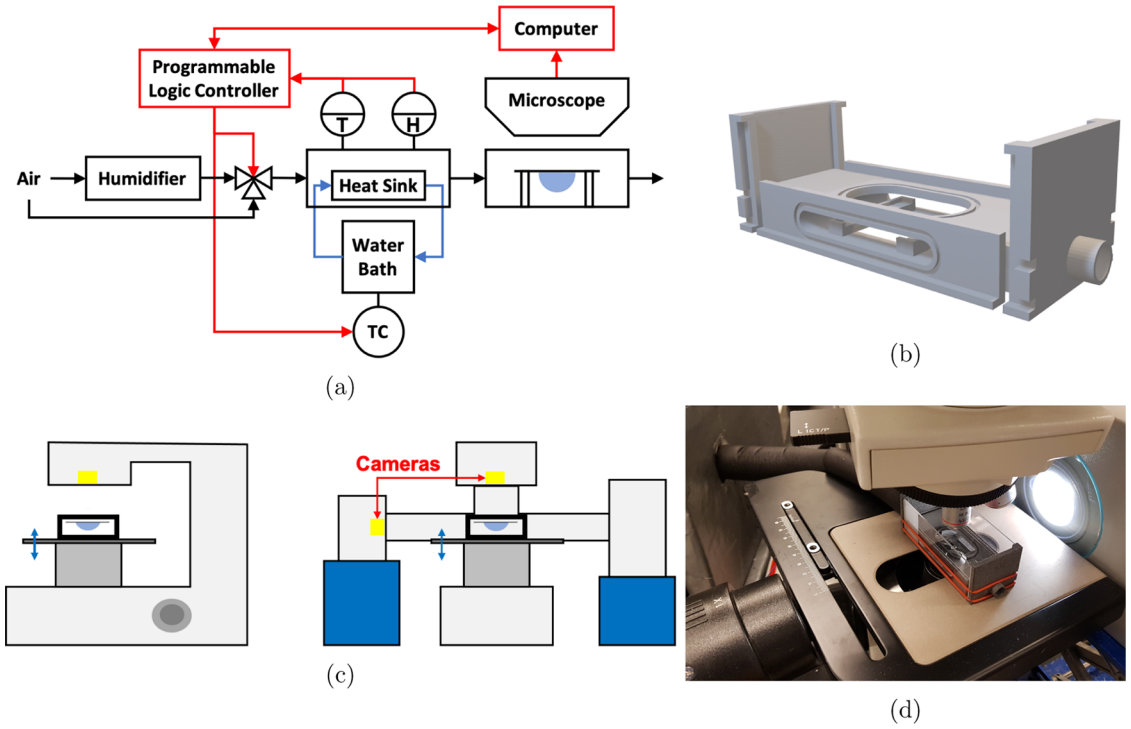

Figure 1. (a) Schematic diagram of the droplet-based evaporation crystallization system. Black lines indicate air flow, blue lines indicate fluid flow, and red lines indicate information flow. (b) 3D drawing view of the designed flow cell in SolidWorks. (c) Schematic diagram of the designed dual-angle in situ imaging system. (d) Photo of the flow cell and the dual-angle in situ imaging system.

and water, and dialysis systems[18] with a flowing precipitant reservoir.

Few studies consider operation at the production scale or characterize the crystallization kinetics needed for systematic scale-up to that scale. A limited quantity of protein is available during the initial stage of process development, which motivates the development of small-scale experimental systems with the capability of collecting experimental data of sufficient quantity and quality for the estimation of crystallization kinetics. This article describes the design of a droplet-based evaporative system for the evaluation of candidate crystallization conditions and the estimation of kinetics using only a minimum quantity of protein. In the developed system, air of controlled temperature and humidity is fed to a flow cell containing the droplet of protein solution to control evaporation and rehydration of the droplet, which are used to manipulate supersaturation. Dual-angle in situ images of the droplet are taken and analyzed to provide on-line measurements of droplet volume and crystal sizes. These measurements are used to estimate crystallization kinetics based on a first-principles model developed for the droplet system. The developed droplet-based evaporative crystallization system is experimentally demonstrated for the model protein lysozyme, which has well-characterized solubility and crystallization kinetics.

2. MATERIALS AND METHODS

2.1. Materials. Protein stock solutions (4, 10, 15, and 35 g/L) were prepared by dissolving hen egg white lysozyme (Hampton Research) in 50 mM citrate buffer, obtained from citric acid and sodium hydroxide (Sigma-Aldrich), at pH 4.5. Citrate buffer was used instead of acetate buffer, which is the most commonly used buffer for lysozyme crystallization because the volatile acetate buffer can evaporate during the operation. The concentration of the protein stock solution was determined by absorbance measurements at 280 nm (Thermo Scientific, NanoDrop One). Precipitant stock solutions (0.5 and 2.5 M) were prepared by dissolving sodium chloride (Sigma-Aldrich) in the citrate buffer. Both solutions were sterile-filtered through 0.22 μm polyethersulfone membranes (Corning). Solutions with target protein and precipitant concentration were prepared by mixing the protein and precipitant stock solutions.

2.2. Solubility Test. The solubility test was performed similarly as a study in the literature.[19] The solubility of lysozyme in 50 mM citrate buffer at pH 4.5 was measured with respect to the concentration of sodium chloride. Supersaturated solutions for solubility measurements with sodium chloride concentrations from 0.25 to 1.25 M were prepared by mixing the protein and precipitant stock solutions. The supersaturated solutions were then stored at 4 °C for 1−3 days to initiate nucleation and grow crystals. The resulting solutions with crystals were placed in an incubating/cooling shaker (VWR) at 25 °C under extensive shaking with 500 rpm. Increasing the concentration of lysozyme in the solutions due to redissolving crystals was monitored periodically by absorbance measurements at 280 nm until equilibrium was reached (3−5 days). The standard deviations were calculated from three independent experiments for each concentration of sodium chloride.

2.3. System Prototype. The process flow diagram of the droplet-based evaporative crystallization system is shown in Figure 1a. A droplet containing aqueous protein solution was hung on the siliconized glass cover slide (Hampton Research) inside an optically visible flow cell for the real-time imaging using microscopes. The flow cell was designed in SolidWorks (Figure 1b) (available for download[20]) and 3D-printed with a HP Multi Jet Fusion PA12 (92 × 29 × 34 mm, Sculpteo). Air of controlled temperature and humidity in a chamber was continuously fed to the flow cell for controlled evaporation and rehydration of the droplet. The humidity in the chamber was controlled by manipulating the ratio of the flow rates of wet air from a designed humidifier and dry air from a separate supply by using a three-way solenoid pinch valve (Masterflex). The temperature in the chamber was controlled by manipulating the set-point temperature of water in a programmable circulating water bath

https://doi.org/10.1021/acs.cgd.1c00231
Cryst. Growth Des. 2021, 21, 6064−6075

(VWR, model 1197P) that was fed to the heat sink (McMaster, Copper tube) integrated into the chamber. The upstream chamber and line to the flow cell were strongly insulated to minimize thermal losses, which would allow the temperature of the air to the flow cell to be set as low as a few degrees above freezing. Evaporation and rehydration were used as handles for dynamically increasing and decreasing the supersaturation, which is the driving force for crystallization.

A programmable logic controller (PLC, Koyo Click CC0-12DRE-1-D) was used for low-level control of the system. The programmable circulating water bath was connected and actuated using the RS-232 port, while the three-way solenoid pinch valve was connected and actuated using the discrete relay output. The relative humidity/temperature transmitter (Omega, model HX15) was connected using the analogue current input. Proportional integral control was designed using the internal model control method[21] and programmed in the PLC for control of the humidity and temperature. The PLC was connected via MODBUS TCP to a computer for data collection and human−machine interface.

A schematic diagram of the designed dual-angle in situ imaging system is shown in Figure 1c. The horizontal-view images were obtained using a microscope (OMAX, model V331A) with a camera (The Imaging Source, model DFK 22BUC03). The vertical-view images were obtained using a microscope (Leica, model DM2500) with a camera (Sony, model ILCE-5100). The cameras were connected via USB to the computer for data collection. The images were then analyzed on-line to obtain the droplet volume and crystal sizes.

2.4. Crystallization Experiment. A 5 μL droplet of solution with a protein concentration of 2.0 g/L and a precipitant concentration of 0.25 M was pipetted on a siliconized glass cover slide, immediately inverted, and placed in the flow cell. Then, the flow cell was sealed with glass slides, o-rings, and rubber bands (Figure 1d). Evaporation and rehydration of the droplet were carried out at a controlled temperature and relative humidity. The droplet was monitored periodically with the imaging system for the droplet volume and crystal sizes.

2.5. Image Analysis Algorithms. The key steps of an on-line algorithm for analyzing the horizontal view images are schematized in Figure 2. The raw image (Figure 2a) is first filtered with a high-pass 2D spatial Gaussian filter to de-background and thresholded to obtain a black-and-white image (Figure 2b). Then, morphological closing and opening are performed to close any openings in the boundary and clear the area around the boundary (Figure 2c). Finally, the 2D convex hull is constructed from the detected boundary, and the top boundary is flattened for a more realistic shape (Figure 2d). The volume of the droplet is calculated with the detected boundary assuming rotational symmetry

$$V = \frac{\pi}{4}\int_{z_0}^{z_h} d^2(z)\,\mathrm{d}z \approx \frac{\pi}{4}\sum_{i=1}^{n_z} {d_i}^2 \Delta z \tag{1}$$

where z_0 is the height of the top of the boundary, z_h is the height at the bottom of the boundary, $d(z)$ is the diameter at height z, and n_z is the number of discretization points. The image analysis software is available for download.[20]

A schematic of the key steps of the on-line algorithm for analyzing the vertical-view images is in Figure 3. The raw image (Figure 3a) is again filtered and thresholded (Figure 3b), and the detected areas around the droplet boundary are removed (Figure 3c). Morphological closing is performed to close any openings in the boundaries, and then holes in the boundaries are filled (Figure 3d). Finally, morphological opening is performed to remove areas smaller than the threshold size (Figure 3e) to obtain the areas of the detected crystals (Figure 3f). The image analysis software is available for download.[20] The threshold size is chosen as 3 pixels to remove the remaining background noise. The pixel size of the vertical-view images is 1.955 μm/pixel, which results in a minimal crystal size detectable of 5.865 μm.

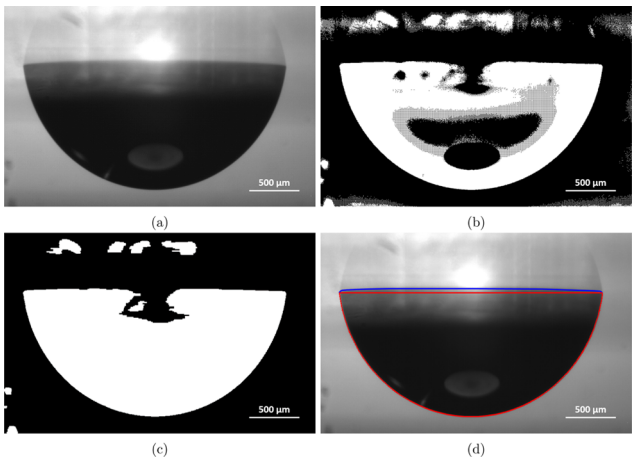

Figure 2. Summary of the designed image analysis algorithm for the horizontal view images. (a) Raw images are (b) filtered with a high-pass 2D spatial Gaussian filter and thresholded. (c) Morphological closing and opening are performed. (d) The 2D convex hull is constructed and the top boundary is flattened.

3. MODEL DEVELOPMENT

3.1. Solubility. The protein solubility is changed during evaporation/rehydration due to change in the concentration of precipitants in the droplet. At low ionic strength, salting-in based on the electrostatic interactions increases the solubility when the ionic strength increases. At high ionic strength, salting-out based on the hydrophobic interactions decreases the solubility when ionic strength increases. These relationships are typically modeled as[22]

$$\ln \frac{C_{\mathrm{P,sat}}}{C_{\mathrm{P,sat,0}}} = k_{\mathrm{i}}\sqrt{I} - k_{\mathrm{o}} I \tag{2}$$

where the ionic strength is given by

$$I = \frac{1}{2}\sum_{\mathrm{S_i}\in \mathbf{S}} {z_{\mathrm{S,i}}}^2 C_{\mathrm{S,i}} \tag{3}$$

$C_{\mathrm{P,sat}}$ is the protein solubility in the solution, $C_{\mathrm{P,sat,0}}$ is the protein solubility in pure water, k_{i} is the salting-in constant, k_{o} is the salting-out constant, $z_{\mathrm{S,i}}$ is the charge, and $C_{\mathrm{S,i}}$ is the concentration of the salt ion $\mathrm{S_i}$, and $\mathbf{S}$ is the set of salt ions in the solution.

For lysozyme, salting-in is not observed at a low ionic strength over a large range of pH due to a predominant electrostatic screening of the positively charged protein and adsorption of salt ions by the protein.[23] In addition, the salting-out behavior of lysozyme observed in the experiments and reported in the literature is not consistent with eq 2.[19,23,24] The observed behavior of lysozyme can be described by the phase equilibrium condition of the protein between the solution and solid in terms of chemical potentials. Then, the protein solubility is expressed as[19,25]

$$\ln C_{\mathrm{P,sat}} = a - b \ln I - cI \tag{4}$$

where a, b, and c are solubility constants. This expression does not account for the change of the chemical potential of the protein in the solid phase but has been shown to correlate well with lysozyme solubility data.[19]

3.2. Crystal Growth. Lysozyme is observed to crystallize in the tetragonal structure,[26] which has two characteristic lengths:

https://doi.org/10.1021/acs.cgd.1c00231
Cryst. Growth Des. 2021, 21, 6064−6075

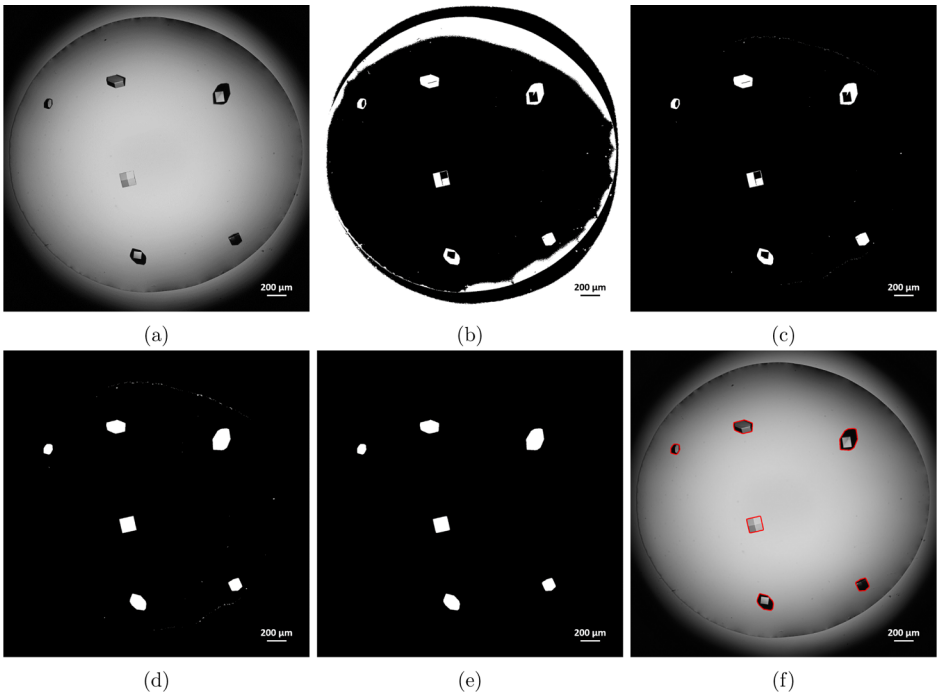

Figure 3. Summary of the designed image analysis algorithm for the vertical view images. (a) Raw images are (b) filtered with a high-pass 2D spatial Gaussian filter and thresholded. (c) Detected areas around the droplet boundary are removed. (d) Morphological closing is performed and holes in the boundaries are filled. (e) Morphological opening is performed. (f) Areas of the crystals are detected.

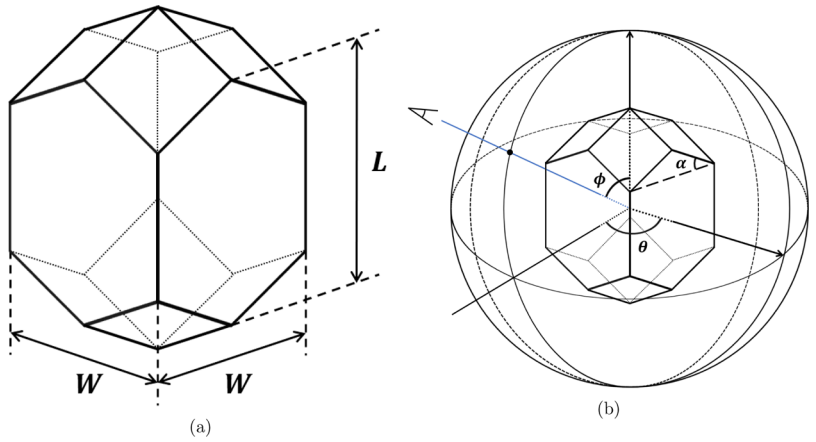

Figure 4. (a) Tetragonal structure of lysozyme crystals with characteristic lengths L and W and (b) observation angles θ and ϕ.

L and W (Figure 4a). With the given crystal structure, the volume of the crystal is

$$V_C = W^2 L \tag{5}$$

The projected area of the crystal measured from the vertical-view images depends on observation angles θ and ϕ (Figure 4b)

$$A_C = WL(\cos\theta + \sin\theta)\sin\phi + \frac{W^2}{4}(2\cos\phi - 2\sin\theta \sin\phi\tan\alpha + |\cos\phi - (\cos\theta + \sin\theta)\sin\phi\tan\alpha| + |\cos\phi - (\cos\theta - \sin\theta)\sin\phi\tan\alpha|) \tag{6}$$

where α is the angle in the hexagon (see the Supporting Information for details). From molecular orientations of the crystal structure,[26] $\tan\alpha = (37.9\ \text{Å})/(4 \times 28\ \text{Å})$. The observation angles are within the ranges $0 \le \theta \le \pi/4$ and $0 \le \phi \le \pi/2$ due to symmetry of the crystal structure.

The protein crystal growth in the droplet is described by a deterministic model for crystal sizes and solution mass balances

$$\frac{dL_n}{dt} = \begin{cases} 0, & \text{if } t < t_n, \\ G_L, & \text{otherwise,} \end{cases} \quad n = 1, \ldots, N \tag{7}$$

$$\frac{dW_n}{dt} = \begin{cases} 0, & \text{if } t < t_n, \\ G_W, & \text{otherwise,} \end{cases} \quad n = 1, \ldots, N \tag{8}$$

$$\frac{dC_P}{dt} = \frac{1}{V}\left(JC_P - \rho_{c,P}\sum_{n=1}^{N}(W_n^2 G_L + 2W_n L_n G_W)\right) \tag{9}$$

https://doi.org/10.1021/acs.cgd.1c00231
Cryst. Growth Des. 2021, 21, 6064−6075

Table 1. Solubility Measurements of Lysozyme in 50 mM Citrate Buffer at pH 4.5 and 25 °C

C_S [M]	0.25	0.50	0.75	1.00	1.25
$C_{P,sat}$ [g/L]	27.46 ± 0.16	8.53 ± 0.03	3.41 ± 0.03	1.80 ± 0.02	1.20 ± 0.02

$$\frac{dC_S}{dt} = \frac{JC_S}{V} \tag{10}$$

$$\frac{dV}{dt} = -J \tag{11}$$

where C_P is the protein concentration, C_S is the salt concentration, V is the droplet volume, G_L and G_W are crystal growth rates, t_n is the time when at least n crystals have nucleated, N is the number of crystals, $\rho_{c,p}$ is the density of protein in a protein crystal, and J is the evaporation rate. The overall density of a protein crystal is the sum of the density of its components (protein p, bound water w, and free solvent s)[27]

$$\rho_c = \sum_{i=p,w,s} \rho_{c,i} = \sum_{i=p,w,s} \phi_i \rho_i \tag{12}$$

where ϕ is the volume fraction, ρ is the apparent density, and the subscripts i refer to the components. For lysozyme, $\rho_{c,p} \approx 0.73$ g/mL was determined from $\rho_{c,p} + \rho_{c,w} \approx 0.88$ g/mL, $\phi_s \approx 0.34$, and $1/\rho_p \approx 0.70$ mL/g.[28]

The crystal growth is observed to be dominated by a continuous spiral growth from screw dislocation at low supersaturation and by two-dimensional nucleation and subsequent growth at high supersaturation.[29,30] Because two-dimensional nucleation was observed to remain as a viable growth mechanism even at low supersaturation for lysozyme,[31,32] the crystal growth rate is modeled by the birth-and-spread model[33,34]

$$G_L = k_{L,1}(S-1)^{2/3}(\ln S)^{1/6} \exp\left(-\frac{k_{L,2}}{\ln S}\right) \tag{13}$$

$$G_W = k_{W,1}(S-1)^{2/3}(\ln S)^{1/6} \exp\left(-\frac{k_{W,2}}{\ln S}\right) \tag{14}$$

where $S = C_P/C_{P,sat}$ is the supersaturation and k_L and k_W are growth rate constants.

3.3. Nucleation. The nucleation of the first protein crystal in the droplet is described by the stochastic model[7,35]

$$\frac{dP_0}{dt} = -B_0(C_{P,0})VP_0, \qquad P_0(0) = 0 \tag{15}$$

$$\frac{dC_{P,0}(t)}{dt} = \frac{J}{V}C_{P,0}, \qquad C_{P,0}(0) = C_P(0) \tag{16}$$

where P_0 is the time evolution of the probability that the droplet contains no crystals and $B_0(C_{P,0})$ is the nucleation rate at the protein concentration $C_{P,0}$ when the droplet contains no crystals. Then, the cumulative distribution function (CDF), the probability distribution function (PDF), and the mean time when at least one crystal has nucleated are[7,35]

$$F_1(t) = P(T_1 \le t) = 1 - P_0(t) \tag{17}$$

$$f_1(t) = \frac{dF_1(t)}{dt} = B_0(C_{P,0})VP_0 \tag{18}$$

$$\bar{t}_1 = \int_0^\infty t f_1(t)\,dt = \int_0^\infty t B_0(C_{P,0})VP_0\,dt \tag{19}$$

where T_i is the random variable for the time when at least i crystals have nucleated.

For the nucleation of subsequent crystals, the protein concentration decreases as already nucleated crystals grow to deplete the protein from the solution. The nucleation of the subsequent crystals can be described by

$$\frac{dP_n}{dt} = -B_0(C_{P,n})VP_n, \qquad P_n(t_n) = 1 \tag{20}$$

$$\frac{dC_{P,n}(t)}{dt} = \frac{1}{V}\left(JC_{P,n} - \rho_{c,p}\sum_{i=1}^{n}(W_i^2 G_L + 2W_i L_i G_W)\right),$$
$$C_{P,n}(t_n) = C_{P,n-1}(t_n) \tag{21}$$

where P_n is the time evolution of the probability that the droplet contains n crystals, and $C_{P,n}$ is the protein concentration when the droplet contains n crystals given that $T_i = t_i$, $i = 1, ..., n$. Then, the CDF, PDF, and mean time when at least $n+1$ crystals have nucleated, given that the $(n+1)$th crystal has nucleated and $T_i = t_i$, $i = 1, ..., n$, are

$$F_{n+1}(t) = P(T_{n+1} \le t | T_{n+1} \in \mathbb{R},\ T_i = t_i,\ i = 1, ..., n)$$
$$= \frac{P(T_{n+1} \le t | T_i = t_i,\ i = 1, ..., n)}{P(T_{n+1} \in \mathbb{R} | T_i = t_i,\ i = 1, ..., n)} = \frac{1 - P_n(t)}{1 - P_n(\infty)} \tag{22}$$

$$f_{n+1}(t) = \frac{dF_{n+1}(t)}{dt} = \frac{B_0(C_{P,n})VP_n(t)}{1 - P_n(\infty)} \tag{23}$$

$$\bar{t}_{n+1} = \int_{t_n}^\infty t f_{n+1}(t)\,dt = \frac{\int_{t_n}^\infty t B_0(C_{P,n})VP_n(t)\,dt}{1 - P_n(\infty)} \tag{24}$$

The primary nucleation rate is modeled by the expression from the classical theory of nucleation[7,36]

$$B_0(C_{P,n}) = k_{B,1}C_{P,n}\exp\left(-\frac{k_{B,2}}{(\ln S_n)^2}\right) \tag{25}$$

where $k_{B,1}$ and $k_{B,2}$ are nucleation parameters and $S_n = C_{P,n}/C_{P,sat}$ is the supersaturation. Although primary nucleation for some systems follows an alternative mechanism known as two-step nucleation,[37] the above expression has been observed to closely fit the experimental nucleation data for most systems.[38]

4. RESULTS AND DISCUSSION

4.1. Solubility. The solubility of lysozyme in acetate buffer is extensively studied in the literature. For droplet-based evaporative crystallization, the volatility of the acetate buffer is not appropriate as it would evaporate from the droplet during operation. In this study, a non-volatile citrate buffer is used instead. The solubility of lysozyme was measured for a sodium chloride concentration from 0.25 to 1.25 M (Table 1). The solubility constants were estimated with least squares (a = 2.02, b = 1.19, c = 1.42) and the solubility of lysozyme at

https://doi.org/10.1021/acs.cgd.1c00231
Cryst. Growth Des. 2021, 21, 6064−6075

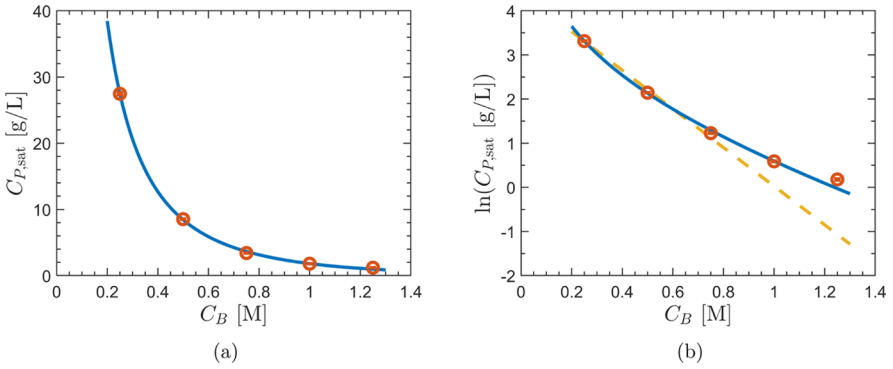

Figure 5. Model predictions (solid line) and experimental data (open circles) for the solubility of lysozyme in 50 mM citrate buffer at pH 4.5 and 25 °C. The additional dashed line shows the model prediction fitted with $b = 0$.

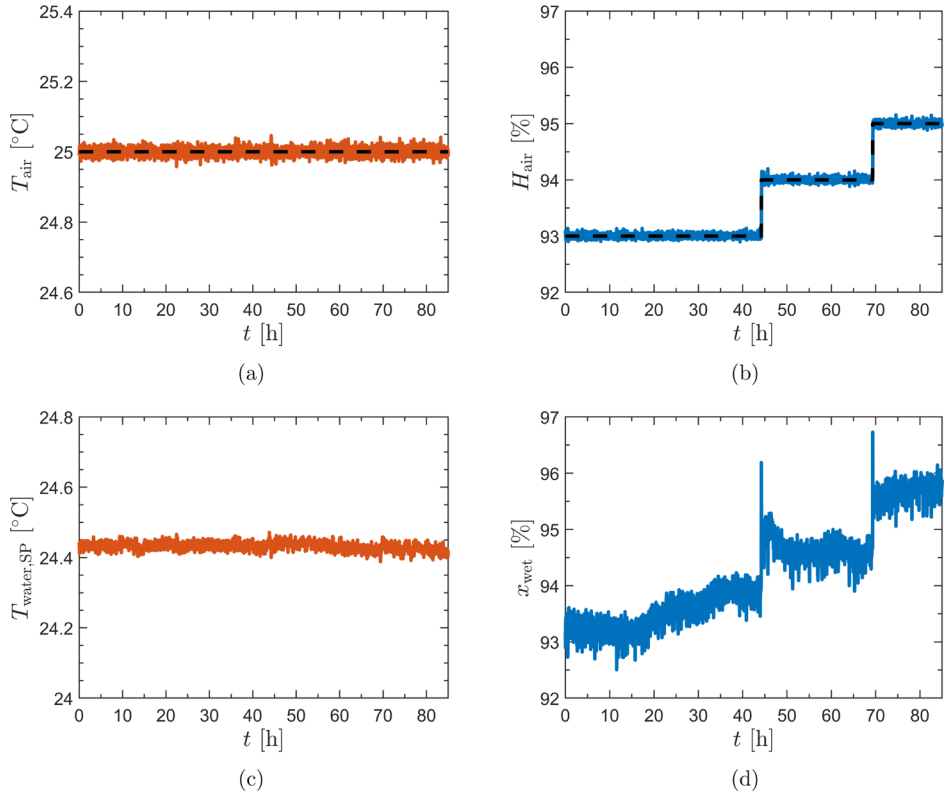

Figure 6. (a) On-line temperature (T_{air}) and (b) relative humidity (H_{air}) measurements of air in the chamber that was continuously fed to the flow cell. Black dashed lines indicate set-points. (c) Set-point temperature of water in the programmable circulating water bath ($T_{\mathrm{water,SP}}$) was manipulated to control the temperature. (d) Wet air fraction (x_{wet}) was manipulated with a three-way solenoid pinch valve to control the relative humidity.

different precipitant concentrations was well described by the model prediction, with a root-mean-squared error (rmse) of 0.15 g/L (Figure 5). Figure 5b shows that the solubility of lysozyme is not described by the commonly used linear salting-out term.

4.2. System Demonstration. Droplet-based evaporative crystallization experimentation was performed with an initial droplet condition of lysozyme concentration $C_{\mathrm{P}}(t = 0) = 2.0$ g/L and sodium chloride concentration $C_{\mathrm{S}}(t = 0) = 0.25$ M. Air flowing into the flow cell was controlled with set-points of temperature $T_{\mathrm{air,SP}} = 25$ °C and relative humidity $H_{\mathrm{air,SP}} = 93\%$. During operation, the set-point of the relative humidity was changed to $H_{\mathrm{air,SP}} = 94\%$ at ~45 h and $H_{\mathrm{air,SP}} = 95\%$ at ~70 h.

The controllers designed for the system responded quickly and accurately with no instability for tracking the set-points of both temperature and relative humidity of the air fed to the flow cell (Figure 6a,b). The system manipulated the set-point temperature of the water circulated to the heat sink in the chamber to be slightly lower than the set-point temperature of air (~0.6 °C) to cool the warm wet air from the humidifier (Figure 6c). The wet air ratio manipulated by the three-way solenoid valve was similar to the set-point relative humidity of the air (difference within 1%), which means that the absolute humidity of the warm wet air from the humidifier was almost same as that of the saturated air at the set-point temperature (Figure 6d).

The system took horizontal-view images every 12 s during the operation, which were analyzed on-line to obtain the droplet volume as described in Section 2.5 (Figure 7a). First, the droplet evaporates until reaching equilibrium with the air at

https://doi.org/10.1021/acs.cgd.1c00231
Cryst. Growth Des. 2021, 21, 6064−6075

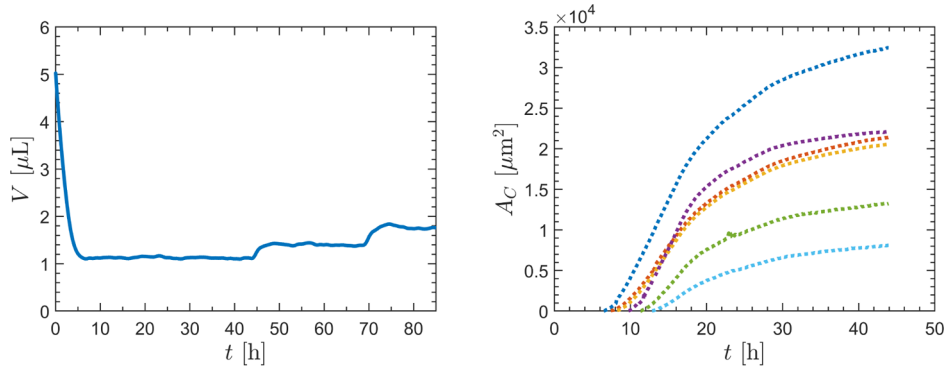

Figure 7. (a) On-line volume measurements of the droplet in the flow cell and (b) projected area measurements of the crystals in the droplet from the image analysis algorithm.

93% relative humidity (Figure 8a,b). Then, as the relative humidity was increased to 94 and 95%, the droplet rehydrates

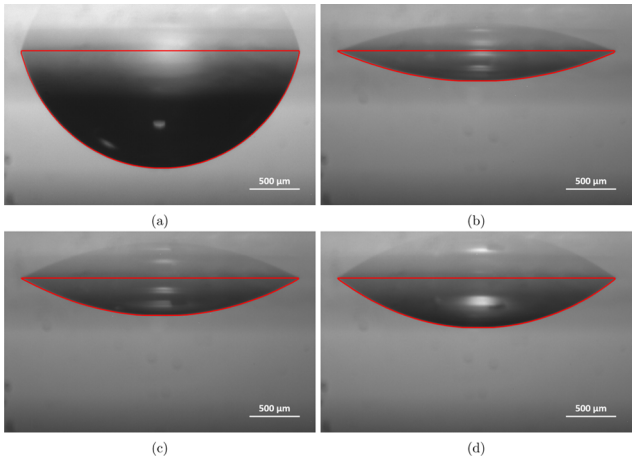

Figure 8. Analyzed horizontal view images at (a) 0 h, (b) 40 h, (c) 65 h, and (d) 80 h.

to equilibrate with the air at increased relative humidity (Figure 8c,d). The equilibrated volume of the droplet measured at each relative humidity is larger than the value calculated from the water activity of sodium chloride solutions in the literature[39] (Figure 9a), which means that the equilibrated concentration of sodium chloride is lower than expected (Figure 9b). These differences are due to a slight decrease of the air temperature as it flows through the flow cell, resulting in an increase in the relative humidity. Because the water activity of sodium chloride solution is nearly independent of temperature of around 25 °C,[40] this slight decrease in air temperature does not affect the expected values derived from the water activity of sodium chloride solutions. The equilibrated volume and concentration of sodium chloride agree well with the expected values when the relative humidity is adjusted with a 0.5 °C decrease in the air temperature (Figure 9a,b), which demonstrates that the rotational symmetry for calculating the volume of the droplet is a reasonable assumption.

Vertical-view images are taken every 5 min during the operation in the system and analyzed on-line to obtain the projected areas of the crystals (Section 2.5). The first crystal was detected at ~6.5 h, subsequently resulting in a total of six crystals in the droplet (Figure 7b). Accurate detection of crystals from the images at various time points demonstrates the generality of the image analysis algorithm (Figure 10). Although all crystals have the same tetragonal structure, they appear as different shapes in the vertical-view images due to different observation angles (Section 3.2). Different growth trends are observed for some projected area of crystals because the crystal growth rates for the two characteristic lengths L and W have different supersaturation dependences.[29]

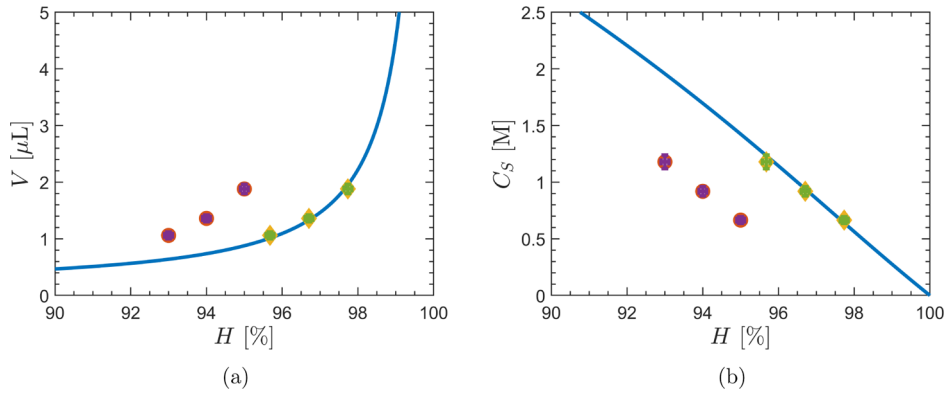

Figure 9. (a) Equilibrium volume of the droplet and (b) concentration of sodium chloride in the droplet as a function of relative humidity. Solid lines are expected values derived from water activities of sodium chloride solutions.[39] Circles are experimental data and diamonds are experimental data adjusted with a 0.5 °C decrease in the air temperature.

https://doi.org/10.1021/acs.cgd.1c00231
Cryst. Growth Des. 2021, 21, 6064−6075

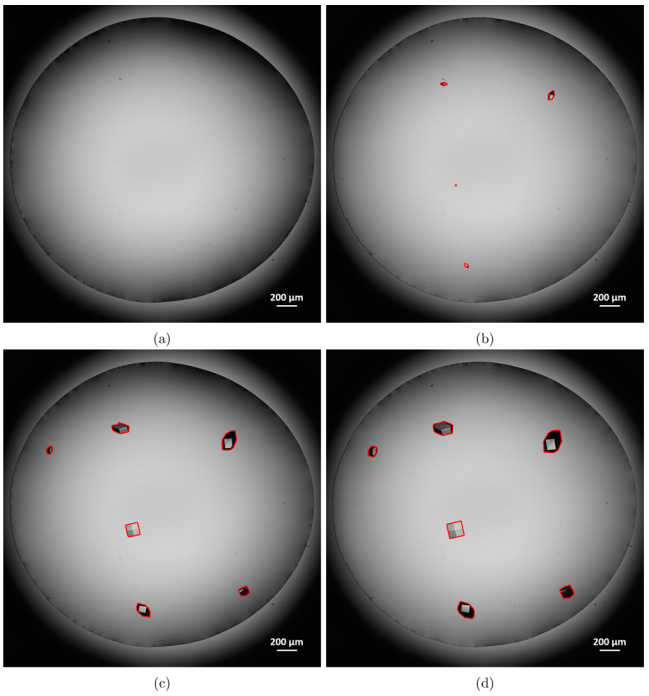

Figure 10. Analyzed vertical view images at (a) 5 h, (b) 10 h, (c) 20 h, and (d) 40 h.

4.3. Crystallization Kinetics Estimation. Measurements of the volume of the droplet and the projected areas of the crystals were used to estimate the crystal growth kinetics. The model predictions with estimated crystal growth kinetics are compared with the crystal projected area measurements in Figure 11. The evaporation rates during the operation were calculated from the droplet volume measurements. The parameters for the crystal growth were estimated by least squares (Table 2). The covariance of the parameter estimates were computed by

$$V_\theta \approx \left(\frac{\partial x(\theta)}{\partial \theta}^{\mathrm{T}} V_\epsilon^{-1} \frac{\partial x(\theta)}{\partial \theta} \right)^{-1}, \quad V_\epsilon = \left(\frac{(y - x(\theta))^{\mathrm{T}} (y - x(\theta))}{n - 1} \right) I_n \tag{26}$$

where $x(\theta)$ is the vector of estimated states that depend on the vector of parameters θ, y is the vector of measured states, and n is number of experimental data points. The sensitivities of the states with respect to the parameters were computed via sensitivity equations.[41] The correlation of parameter estimates are given by (Table 3)

$$R_{\theta,ij} = \frac{V_{\theta,ij}}{\sqrt{V_{\theta,ii} V_{\theta,jj}}} \tag{27}$$

The projected area measurement data of the crystals at different supersaturation conditions are well described by the model, with an rmse of 170 μm^2, which is within 0.5−2.5% of the measured crystal projected areas. The estimated crystal growth kinetics capture the different dependencies of the two characteristic lengths L and W on supersaturation, as has been reported in the literature[29] (Figure 12a). These different dependencies are also consistent with the on-line crystal images. Vertical-view images for the second crystal during the

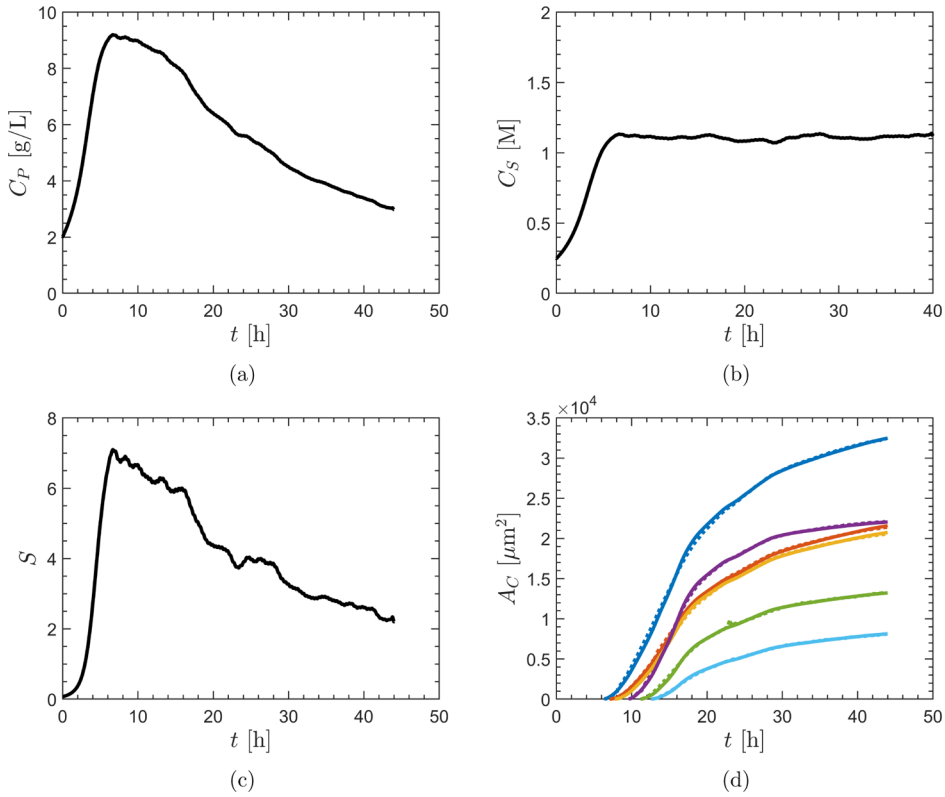

Figure 11. Model predictions (solid lines) and experimental data (dotted lines) for (a) protein concentration, (b) salt concentration, (c) supersaturation, and (d) projected crystal areas.

https://doi.org/10.1021/acs.cgd.1c00231
Cryst. Growth Des. 2021, 21, 6064−6075

Table 2. Estimated Values of Parameters for Crystallization Kinetics

$k_{L,1}$ [μm/h]	$k_{L,2}$	$k_{W,1}$ [μm/h]	$k_{W,2}$
0.752 ± 0.009	(7.05 ± 1.77) × 10^{-2}	(1.50 ± 0.34) × 10^{3}	10.5 ± 0.1

Table 3. Correlations of the Estimated Parameters for the Crystal Growth Kinetics

	$k_{L,1}$	$k_{L,2}$	$k_{W,1}$	$k_{W,2}$
$k_{L,1}$	1	0.985	−0.855	−0.860
$k_{L,2}$	0.985	1	−0.761	−0.768
$k_{W,1}$	−0.855	−0.761	1	0.999
$k_{W,2}$	−0.860	−0.768	0.999	1

operation are shown in Figure 13. Due to the observation angles, the vertical line across the projected area denotes the characteristic length L and the horizontal line across the projected area denotes the characteristic length W. Initially, when supersaturation was high, the growth rate of W was faster than the growth rate of L and the horizontal distance across the crystal grew more than the vertical distance (Figure 13a−c). However, as supersaturation decreased over time, the growth rate on the crystal length L became faster and the vertical distance across the crystal grew more than the horizontal distance (Figure 13c−e).

The estimated crystal growth kinetics are compared with the experimental studies in the literature[42−45] in Figure 12b. Although this study was performed in citrate buffer and all experimental studies in the literature were performed in acetate buffer, the estimated growth rate is within the variation of the values reported in the literature.

The estimated crystal growth kinetics were used with the experimental measurements to estimate the crystal nucleation kinetics. Figure 14 compares the resulting model predictions with the measured times when crystals nucleated. The kinetic parameters for crystal nucleation were estimated by least squares to be $\ln(k_{B,1}, g^{-1}\ h^{-1}) = 20.4$ and $k_{B,2} = 17.3$. The induction times measured in the experiments are well described by the model. The estimated kinetic parameters indicate faster kinetics and larger dependence on supersaturation compared to the literature, which reported $\ln(k_{B,1}, g^{-1}\ h^{-1}) = 12.5$ and $k_{B,2} = 9.7$.[35] The differing nucleation rates could be due to differing buffers or pH but are mostly dominated by change in the pH. The study in the literature started the experiment at pH 4.6, but the pH would have increased during the experiment as acetate would have evaporated with the water. The nucleation rate of tetragonal lysozyme crystals is known to have a noticeable effect by the solution pH. The change of pH from 4.6 to 4.8 is reported to result in a drop in the nucleation rate by a factor of about 20, which is a significant change over a very narrow range.[46]

5. CONCLUSIONS

A droplet-based evaporative system is described for evaluating crystallization conditions and estimating kinetics using only a droplet of protein solution (on the order of microliters). The system feeds air of controlled temperature and humidity to a flow cell containing the droplet to control evaporation and rehydration of the droplet and consequently the supersaturation. The horizontal- and vertical-view images of the droplet are collected by a dual-angle in situ imaging system and analyzed on-line to obtain the volume of the droplet and the projected area of the crystals. These on-line measurement data are used to estimate the crystallization kinetics based on a process model for the stochastic crystal nucleation and deterministic crystal growth in the droplet.

Experimentation with the model protein lysozyme demonstrates tight control of the temperature and relative humidity of the air fed to the droplet and fast and accurate image analysis by image analysis algorithms. The equilibrated droplet volume is related by a thermodynamic model to the relative humidity by the water activity of the solution. Although not a focus of this work, this model could be incorporated in a higher-level controller to control the droplet volume by manipulating the set-point of the relative humidity of the air. Projected crystal area measurements and corresponding nucleation induction time measurements show good agreement with a mathematical model that incorporates the crystallization kinetics estimated from data collected by the droplet-based evaporative crystallization system. The system can be used to study the effects of crystallization additives on the solubility and crystallization kinetics.

The capability of the droplet-based evaporative crystallization system to estimate crystallization kinetics using only a

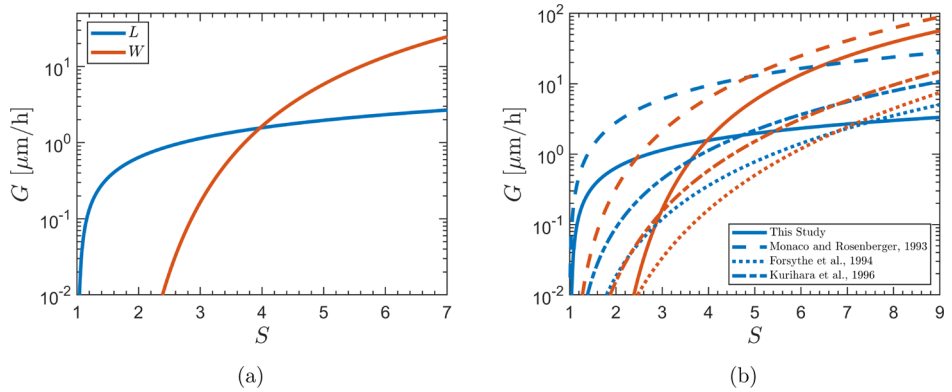

Figure 12. (a) Model predictions for the crystal growth kinetics for the two characteristic lengths L (blue solid line) and W (red solid line). (b) Comparison of growth rates from the model and the literature. Dashed lines,[42] dotted lines,[43] and dash-dotted lines[44] are power law models fit to the experimental literature data.[45]

https://doi.org/10.1021/acs.cgd.1c00231
Cryst. Growth Des. 2021, 21, 6064−6075

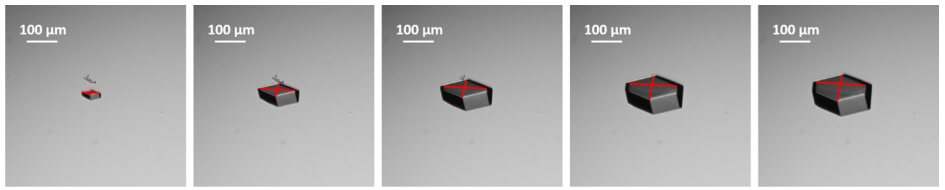

Figure 13. Analyzed vertical-view images of the second crystal at (a) 10 h, (b) 15 h, (c) 20 h, (d) 30 h, and (e) 40 h.

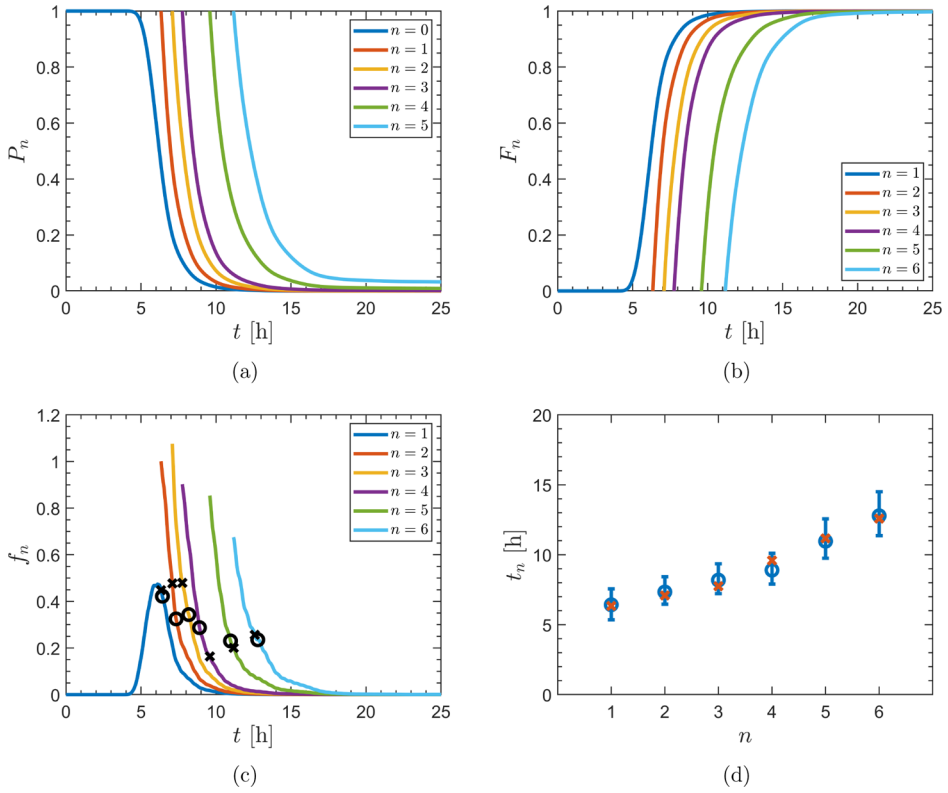

Figure 14. Model predictions (solid lines) of the (a) time evolution of the probability that the droplet contains n crystals, (b) cumulative distribution function, and (c) probability distribution function of the time when at least n crystals have nucleated. The circles denote mean values from the model predictions and the crosses denote experimental data. (d) Model predictions (circles and bars) of mean and 75% prediction interval of the time and experimental data (crosses) of the time when at least n crystals have nucleated.

minimum quantity of protein enables a systematic approach to design and control protein crystallization at the early stage of process development. The estimated crystallization kinetics provide information required for the model-based optimal scale-up to production scale. The crystallization kinetics estimated from the droplet-based system would remain applicable to process models for larger-scale crystallization systems. These population balance models would be augmented with secondary nucleation, aggregation, and breakage rate expressions, where significant, for which physics-based models are available (e.g., ref 47). The population balance model would be combined with computational fluid dynamics if the mixing at the larger scale deviates significantly from ideal conditions (e.g., refs 48 and 49).

■ ASSOCIATED CONTENT

Supporting Information

The Supporting Information is available free of charge at https://pubs.acs.org/doi/10.1021/acs.cgd.1c00231.

Detailed derivation of the projected area of the crystal measured from the vertical-view images (PDF)

■ AUTHOR INFORMATION

Corresponding Author

Richard D. Braatz − *Department of Chemical Engineering, Massachusetts Institute of Technology, Cambridge, Massachusetts 02139, United States;* orcid.org/0000-0003-4304-3484; Email: braatz@mit.edu

Authors

Moo Sun Hong − *Department of Chemical Engineering, Massachusetts Institute of Technology, Cambridge, Massachusetts 02139, United States;* orcid.org/0000-0003-2274-5030

Amos E. Lu − *Department of Chemical Engineering, Massachusetts Institute of Technology, Cambridge, Massachusetts 02139, United States*

Jaehan Bae − *School of Chemical and Biological Engineering, Seoul National University, Seoul 08826, Republic of Korea*

https://doi.org/10.1021/acs.cgd.1c00231
Cryst. Growth Des. 2021, 21, 6064−6075

Jong Min Lee − *School of Chemical and Biological Engineering, Seoul National University, Seoul 08826, Republic of Korea;* orcid.org/0000-0001-5395-0067

Complete contact information is available at: https://pubs.acs.org/10.1021/acs.cgd.1c00231

Notes

The authors declare no competing financial interest.

■ ACKNOWLEDGMENTS

This work was supported by the Bill & Melinda Gates Foundation [OPP1154682]. The findings and conclusions contained within are those of the authors and do not necessarily reflect positions or policies of the Bill & Melinda Gates Foundation. Financial support is acknowledged from the Engineering Development Research Center (EDRC) at Seoul National University for J.B.

■ REFERENCES

(1) Zydney, A. L. Continuous downstream processing for high value biological products: A review. *Biotechnol. Bioeng.* **2016**, *113*, 465−475.
(2) Gupta, P.; Kateja, N.; Mishra, S.; Kaur, H.; Rathore, A. S. Economic Assessment of Continuous Processing for Manufacturing of Biotherapeutics. *Biotechnol. Prog.* **2021**, *37*, No. e3108.
(3) Hong, M. S.; Severson, K. A.; Jiang, M.; Lu, A. E.; Love, J. C.; Braatz, R. D. Challenges and opportunities in biopharmaceutical manufacturing control. *Comput. Chem. Eng.* **2018**, *110*, 106−114.
(4) Shukla, A. A.; Thömmes, J. Recent advances in large-scale production of monoclonal antibodies and related proteins. *Trends Biotechnol.* **2010**, *28*, 253−261.
(5) Thömmes, J.; Etzel, M. Alternatives to chromatographic separations. *Biotechnol. Prog.* **2007**, *23*, 42−45.
(6) Low, D.; O'Leary, R.; Pujar, N. S. Future of antibody purification. *J. Chromatogr. B: Anal. Technol. Biomed. Life Sci.* **2007**, *848*, 48−63.
(7) Hong, M. S.; Kaur, K.; Sawant, N.; Joshi, S. B.; Volkin, D. B.; Braatz, R. D. Crystallization of a nonreplicating rotavirus vaccine candidate. *Biotechnol. Bioeng.* **2021**, *118*, 1750−1756.
(8) Hong, M. S.; Sun, W.; Lu, A. E.; Braatz, R. D. Process analytical technology and digital biomanufacturing of monoclonal antibodies. *Am. Pharm. Rev.* **2020**, *23*, 122−125.
(9) Stevens, R. C. High-throughput protein crystallization. *Curr. Opin. Struct. Biol.* **2000**, *10*, 558−563.
(10) Hui, R.; Edwards, A. High-throughput protein crystallization. *J. Struct. Biol.* **2003**, *142*, 154−161.
(11) Hansen, C. L.; Skordalakes, E.; Berger, J. M.; Quake, S. R. A robust and scalable microfluidic metering method that allows protein crystal growth by free interface diffusion. *Proc. Natl. Acad. Sci. U.S.A.* **2002**, *99*, 16531−16536.
(12) Hansen, C. L.; Classen, S.; Berger, J. M.; Quake, S. R. A Microfluidic Device for Kinetic Optimization of Protein Crystallization andIn SituStructure Determination. *J. Am. Chem. Soc.* **2006**, *128*, 3142−3143.
(13) Zheng, B.; Roach, L. S.; Ismagilov, R. F. Screening of protein crystallization conditions on a microfluidic chip using nanoliter-size droplets. *J. Am. Chem. Soc.* **2003**, *125*, 11170−11171.
(14) Zheng, B.; Tice, J. D.; Roach, L. S.; Ismagilov, R. F. A droplet-based, composite PDMS/glass capillary microfluidic system for evaluating protein crystallization conditions by microbatch and vapor-diffusion methods with on-chip X-ray diffraction. *Angew. Chem., Int. Ed.* **2004**, *43*, 2508−2511.
(15) Talreja, S.; Kim, D. Y.; Mirarefi, A. Y.; Zukoski, C. F.; Kenis, P. J. A. Screening and optimization of protein crystallization conditions through gradual evaporation using a novel crystallization platform. *J. Appl. Crystallogr.* **2005**, *38*, 988−995.
(16) Talreja, S.; Perry, S. L.; Guha, S.; Bhamidi, V.; Zukoski, C. F.; Kenis, P. J. A. Determination of the phase diagram for soluble and membrane proteins. *J. Phys. Chem. B* **2010**, *114*, 4432−4441.
(17) de Wijn, R.; Rollet, K.; Engilberge, S.; McEwen, A.; Hennig, O.; Betat, H.; Mörl, M.; Riobé, F.; Maury, O.; Girard, E.; Bénas, P.; Lorber, B.; Sauter, C. Monitoring the production of high diffraction-quality crystals of two enzymes in real time using in situ dynamic light scattering. *Crystals* **2020**, *10*, 65.
(18) Junius, N.; Oksanen, E.; Terrien, M.; Berzin, C.; Ferrer, J.-L.; Budayova-Spano, M. A crystallization apparatus for temperature-controlled flow-cell dialysis with real-time visualization. *J. Appl. Crystallogr.* **2016**, *49*, 806−813.
(19) Annunziata, O.; Payne, A.; Wang, Y. Solubility of lysozyme in the presence of aqueous chloride salts: Common-ion effect and its role on solubility and crystal thermodynamics. *J. Am. Chem. Soc.* **2008**, *130*, 13347−13352.
(20) Hong, M. S.; Lu, A. E.; Braatz, R. D. *A Droplet-Based Evaporative System for the Estimation of Protein Crystallization Kinetics*; Massachusetts Institute of Technology: Cambridge, MA, 2021. Available: https://github.com/moosun1/Droplet.
(21) Morari, M.; Zafiriou, E. *Robust Process Control*; Prentice-Hall: Englewood Cliffs, NJ, 1989.
(22) Green, A. A. Studies in the Physical Chemistry of the Proteins. *J. Biol. Chem.* **1932**, *95*, 47−66.
(23) Retailleau, P.; Riès-Kautt, M.; Ducruix, A. No salting-in of lysozyme chloride observed at low ionic strength over a large range of pH. *Biophys. J.* **1997**, *73*, 2156−2163.
(24) Ries-Kautt, M. M.; Ducruix, A. F. Relative effectiveness of various ions on the solubility and crystal growth of lysozyme. *J. Biol. Chem.* **1989**, *264*, 745−748.
(25) Annunziata, O.; Paduano, L.; Pearlstein, A. J.; Miller, D. G.; Albright, J. G. The effect of salt on protein chemical potential determined by ternary diffusion in aqueous solutions. *J. Phys. Chem. B* **2006**, *110*, 1405−1415.
(26) Nadarajah, A.; Pusey, M. L. Growth mechanism and morphology of tetragonal lysozyme crystals. *Acta Crystallogr., Sect. D: Biol. Crystallogr.* **1996**, *52*, 983−996.
(27) Colman, P. M.; Matthews, B. W. Symmetry, molecular weight and crystallographic data for sweet potato β-amylase. *J. Mol. Biol.* **1971**, *60*, 163−168.
(28) Leung, A. K. W.; Park, M. M. V.; Borhani, D. W. An improved method for protein crystal density measurements. *J. Appl. Crystallogr.* **1999**, *32*, 1006−1009.
(29) Durbin, S. D.; Feher, G. Crystal growth studies of lysozyme as a model for protein crystallization. *J. Cryst. Growth* **1986**, *76*, 583−592.
(30) Sazaki, G.; Matsui, T.; Tsukamoto, K.; Usami, N.; Ujihara, T.; Fujiwara, K.; Nakajima, K. In situ observation of elementary growth steps on the surface of protein crystals by laser confocal microscopy. *J. Cryst. Growth* **2004**, *262*, 536−542.
(31) Durbin, S. D.; Feher, G. Simulation of lysozyme crystal growth by the Monte Carlo method. *J. Cryst. Growth* **1991**, *110*, 41−51.
(32) Durbin, S. D.; Carlson, W. E. Lysozyme crystal growth studied by atomic force microscopy. *J. Cryst. Growth* **1992**, *122*, 71−79.
(33) Ohara, M.; Reid, R. C. *Modeling Crystal Growth Rates from Solution*; Prentice-Hall: Englewood Cliffs, NJ, 1973.
(34) Myerson, A. S. *Handbook of Industrial Crystallization*; Butterworth-Heinemann: Woburn, MA, 2002.
(35) Goh, L.; Chen, K.; Bhamidi, V.; He, G.; Kee, N. C. S.; Kenis, P. J. A.; Zukoski, C. F.; Braatz, R. D. A stochastic model for nucleation kinetics determination in droplet-based microfluidic systems. *Cryst. Growth Des.* **2010**, *10*, 2515−2521.
(36) Nielsen, A. E. *Kinetics of Precipitation*; Macmillan Co.: New York, 1964.
(37) Erdemir, D.; Lee, A. Y.; Myerson, A. S. Nucleation of crystals from solution: Classical and two-step models. *Acc. Chem. Res.* **2009**, *42*, 621−629.
(38) Kim, K.-J.; Mersmann, A. Estimation of metastable zone width in different nucleation processes. *Chem. Eng. Sci.* **2001**, *56*, 2315−2324.

(39) Tang, I. N.; Tridico, A. C.; Fung, K. H. Thermodynamic and optical properties of sea salt aerosols. *J. Geophys. Res.: Atmos.* **1997**, *102*, 23269−23275.
(40) Chirife, J.; Resnik, S. L. Unsaturated solutions of sodium chloride as reference sources of water activity at various temperatures. *J. Food Sci.* **1984**, *49*, 1486−1488.
(41) Hong, M. S.; Velez-Suberbie, M. L.; Maloney, A. J.; Biedermann, A.; Love, K. R.; Love, J. C.; Mukhopadhyay, T. K.; Braatz, R. D. Macroscopic modeling of bioreactors for recombinant protein producing Pichia pastoris in defined medium. *Biotechnol. Bioeng.* **2021**, *118*, 1199−1212.
(42) Monaco, L. A.; Rosenberger, F. Growth and etching kinetics of tetragonal lysozyme. *J. Cryst. Growth* **1993**, *129*, 465−484.
(43) Forsythe, E.; Ewing, F.; Pusey, M. Studies on tetragonal lysozyme crystal growth rates. *Acta Crystallogr., Sect. D: Biol. Crystallogr.* **1994**, *50*, 614−619.
(44) Kurihara, K.; Miyashita, S.; Sazaki, G.; Nakada, T.; Suzuki, Y.; Komatsu, H. Interferometric study on the crystal growth of tetragonal lysozyme crystal. *J. Cryst. Growth* **1996**, *166*, 904−908.
(45) Liu, J. J.; Ma, C. Y.; Hu, Y. D.; Wang, X. Z. Modelling protein crystallisation using morphological population balance models. *Chem. Eng. Res. Des.* **2010**, *88*, 437−446.
(46) Judge, R. A.; Jacobs, R. S.; Frazier, T.; Snell, E. H.; Pusey, M. L. The effect of temperature and solution ph on the nucleation of tetragonal lysozyme crystals. *Biophys. J.* **1999**, *77*, 1585−1593.
(47) Bermingham, S. K.; Kramer, H. J. M.; van Rosmalen, G. M. Towards on-scale crystalliser design using compartmental models. *Comput. Chem. Eng.* **1998**, *22*, S355−S362.
(48) da Rosa, C. A.; Braatz, R. D. openCrys: Open-source software for the multiscale modeling of combined antisolvent and cooling crystallization in turbulent flow. *Ind. Eng. Chem. Res.* **2018**, *57*, 11702−11711.
(49) Marchisio, D. L.; Vigil, R. D.; Fox, R. O. Quadrature method of moments for aggregation-breakage processes. *J. Colloid Interface Sci.* **2003**, *258*, 322−334.

https://doi.org/10.1021/acs.cgd.1c00231
Cryst. Growth Des. 2021, 21, 6064−6075